Origami-Inspired Robot that Swims via Jet Propulsion

Zhiyuan Yang[1], Dongsheng Chen[1], David J. Levine[1], and Cynthia Sung[1]

***Abstract*—Underwater swimmers present unique opportunities for using bodily reconfiguration for self propulsion. Origami-inspired designs are low-cost, fast to fabricate, robust, and can be used to create compliant mechanisms useful in energy efficient underwater locomotion. In this paper, we demonstrate an origami-inspired robot that can change its body shape to ingest and expel water, creating a jet that propels it forward similarly to cephalopods. We use the magic ball origami pattern, which can transform between ellipsoidal (low volume) and spherical (high volume) shapes. A custom actuation mechanism contracts the robot to take in fluid, and the inherent mechanics of the magic ball returns the robot to its natural shape upon release. We describe the design and control of this robot and verify its locomotion in a water tank. The resulting robot is able to move forward at 6.7 cm/s (0.2 body lengths/s), with a cost of transport of 2.0.**

***Index Terms*—Soft Robot Materials and Design, Marine Robotics, Biologically-Inspired Robots, Mechanism Design**

I. Introduction

SWIMMERS found in nature often use shape change for movement. Soft creatures such as cephalopods (octopus or squid) or jellyfish display natural compliance that enhance their aquatic performance. Among many sea-dwelling organisms, cephalopods have been observed to demonstrate impressive locomotion performance though jet propulsion [1], [2]. This motion is triggered by a rapid change in body cavity volumes, which is enabled by the cephalopod's compliant body and muscular structure. In this paper, we demonstrate an origami-inspired soft swimming robot that simulates this behavior of cephalopods. Leveraging an origami magic ball pattern and tendon-driven actuation, we show that a similar quick volume change and jet propulsion is possible in a swimming robot.

In swimming systems, the morphology of the swimmer strongly impacts its swimming behavior, its speed and trajectory through a flow, and its energy consumption [3]. Two particular major factors that contribute to a cephalopod's locomotion behavior are the vortex-ring based jet propulsion and the added-mass effect caused by change of volume. The vortex-ring based time-dependent jet mode has been shown to be up to 50% more efficient than the continuous steady jet mode [4], indicating that it may actually be preferred to design locomotion strategies that generate unsteady jets. Two distinctive jet modes (the one with a single vortex-ring and the one with a vortex-ring and trailing jet) were discovered experimentally in [5], and a formation number was proposed to characterize the transition point from one mode to the other. It has been verified that certain jet modes are more efficient than others [6] and that squids use these more efficient modes in their own swimming [7]. The shape of the nozzle will affect the jet as well. A converging shape nozzle can generate a higher velocity profile than that a parallel nozzle does [8], [9]. Finally, the added-mass effect, which occurs when a body accelerating through a fluid must effectively move the mass of the fluid in front of it, has also been shown to have either a positive or a negative contribution on thrust and drag force [3], [10] depending on the rate of change in body shape, as described by a shape change number.

Attempts to use shape change in swimming robots span flapping designs imitating biological strategies, *e.g.*, snakes, insects, or manta rays [11], [12], hydraulically-powered fish-like oscillation [13], [14], [15], and octopus-inspired vehicles using jet propulsion [16], [17]. These swimmers often take advantage of soft and stretchable elastomers or fabrics to achieve repeatable reconfigurability [18], thus allowing them to move between the particular morphologies witnessed in biological systems that are capable of high-agility aquatic performance. Soft materials are also safe for operation around animals, humans, and delicate sea structures such as coral reefs, making them ideal for exploring underwater environments and surroundings [15]. Further, soft robotic devices have the potential to reduce manufacturing complexity and cost by taking advantage of monolothic fabrication processes [15]. We take advantage of these same benefits in our origami-inspired robot.

Our work exists in the context of a large number of recent advancements in squid-like robots. An elastomeric shell capable of one-time manually-released jet propulsion was demonstrated in [19]. The effects of shape change on a robot's interactions with its surrounding flow and the possibility of taking advantage of added mass effect were mentioned in [19], [20]. Work in [16], [21] used tendons connected radially to an elastomeric shell to enable repeated propulsive maneuvers, and also proposed kinematic and dynamic models relating volume change and robot velocity. A simpler elastic

Manuscript received: February 24, 2021; Revised May 24, 2021; Accepted June 30, 2021.

This paper was recommended for publication by Editor Kyu-Jin Cho upon evaluation of the Associate Editor and Reviewers' comments. This research was supported in part by a University Research Foundation grant from the University of Pennsylvania. D.J. Levine was supported by a Department of Education GAANN fellowship (Grant No. P200A160282) to the Department of Mechanical Engineering and Applied Mechanics at the University of Pennsylvania.

[1]The authors are with the General Robotics, Automation, Sensing & Perception (GRASP) Laboratory at the University of Pennsylvania, Philadelphia, PA 19104, USA. (annieyzy, dschen, djlev, crsung)@seas.upenn.edu

Digital Object Identifier (DOI): see top of this page.

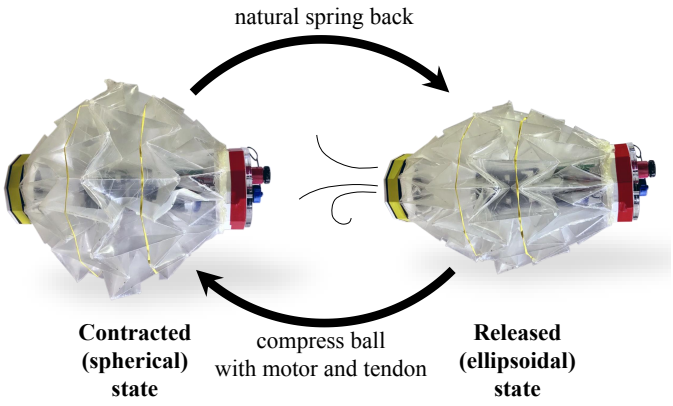

Fig. 1. Robot design concept. The robot is a deformable ball shape that can contract in length into a spherical shape (left). When released, the robot returns to its natural ellipsoidal (right) shape, expelling a jet and propelling itself forward.

beam and shell design was demonstrated in [17], using a slip-gear actuation mechanism to expand and deflate the robot body. In addition, many other locomotion methods have been shown. For example, a novel vortex-ring based underwater robot with the ability to steer itself through soft actuators was demonstrated in [22], and the relation between motor speed and thrust was modeled. Thrust vectoring has been used for steering and to improve robot maneuverability [17], [23]. Finally, soft actuators such as dielectric elastomers have been integrated into robots with more jellyfish-like locomotion [24].

Many of these robots typically leverage elastomeric skins for shape change and require complex fabrication and assembly processes, including casting and molding of precise skin designs such as those in [14], [15], [21], [22], [23], [24]. In contrast to these works, we use an origami skin, which lowers fabrication and assembly time. Since origami patterns can fold from 2D sheets into 3D structures, origami-inspired robots can be assembled and packaged into small sizes for storage, transport, and deployment within a few hours [25], [26]. Due to the compliance of the folded sheets, the mechanical properties and degrees of freedom of the design can be tuned by changing their geometry [27], [28].

A. Our Contributions

We therefore propose an origami-inspired cephalopod-like swimming robot design capable of a jet propulsive maneuver through tendon-driven body shape change. Our robot leverages a magic ball origami pattern to translate length change induced by the motor into volumetric shape change. Further, the modular design of the robot allows different components to be changed quickly and easily, enabling future extensive exploration of the effect of different geometric and mechanics parameters on the robot's locomotive capabilities. We experimentally measure the effect of actuation parameter changes (such as amount of bodily contraction and actuation frequency) on the robot's forward velocity and cost of transport. Our main contributions include:

- the design of an origami-inspired jet-propelled, hydraulic soft swimmer that can achieve repeatable, underwater forward motion;
- the use of a deformable magic ball origami skin for inflation and deflation using a motor and tendon; and
- experimental validation of the robot's swimming performance across a range of actuation parameters, showing the robot can swim forward at 6.7 cm/s (0.20 body lengths/s) with a cost of transport of 2.0.

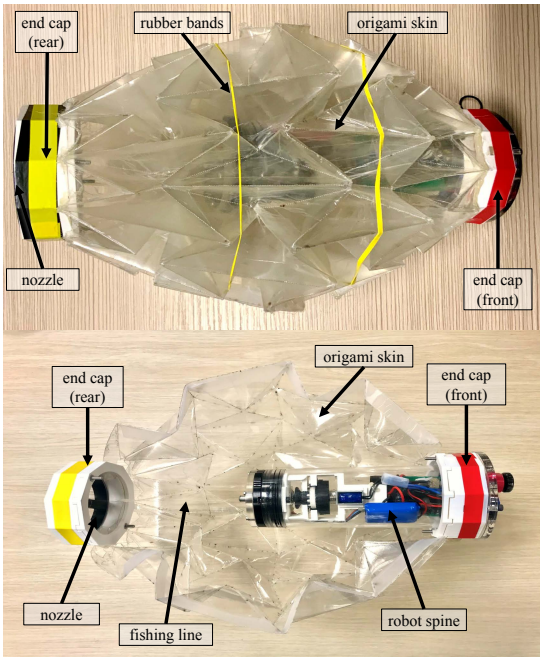

Fig. 2. The robot consists of an origami skin driven by a tendon (fishing line) and DC motor inside the central spine. 3D printed end caps are used to clamp the skin and spine in place. Top: Labeled robot with full skin. Bottom: Section view with the skin cut in half, showing the inner spine and fishing line.

The remainder of this paper is structured as follows. Section II gives an overview of our robot. Section III presents the design of our origami swimming robot and explains fabrication details of the robot. Section IV explains the actuation system and control flow. Section V describes our experimental setup and results. Section VI concludes with a discussion of our results and future work.

II. Origami Swimming Robot Design Overview

Our origami-inspired robot leverages jet propulsion for forward motion. The overall design is shown in Fig. 1. The robot has the ability to expand and contract in order to fill itself with the surrounding water and expel the water quickly, forming a jet that propels itself forward.

Figure 2 shows a high-level breakdown of the robot components. The most important component of the robot is an origami skin that forms the outer surface (ref. Section III). This skin is a magic ball pattern that has the ability to change between an oblong ellipsoidal shape and a spherical shape when compressed or stretched in the longitudinal direction. A waterproof tube 5.08 cm in diameter and 15.0 cm in length forms the central "spine" of the robot and holds the actuators, control electronics, sensors and battery needed to drive the robot between configurations (ref. Section IV). 3D printed

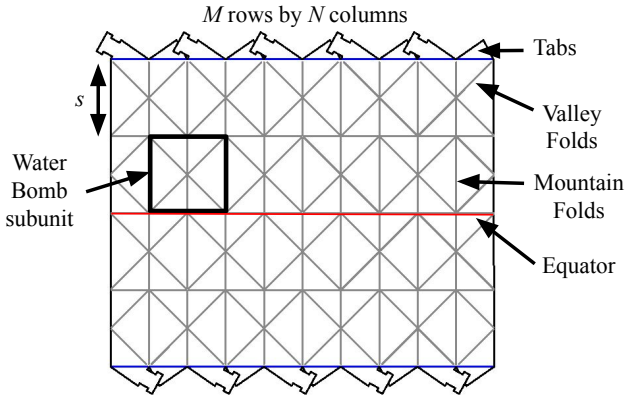

Fig. 3. The origami fold pattern of the robot design. The pattern is a tessellation of water bomb subunits in the magic ball concept. Mountain and valley folds are denoted in gray. The two sides of the pattern are joined together to form a cylindrical shape. Tabs at the top and bottom of the pattern form the connection between the skin and the robot end caps.

end caps at either end of the robot include mounting slots for connecting the origami skin to this spine. A hole in the rear end cap allows water to enter and exit the origami skin. A tendon connecting from the actuation mechanism in the spine to the rear end cap controls the length of the robot. The caps screw to allow the skin to be changed or repaired as needed. Finally, rubber bands can be added around the diameter of the skin to change its stiffness properties. The final assembled robot is 30.5 cm in length and 19 cm in diameter in its ellipsoidal form (25 cm in length, 23 cm in diameter in spherical form) and weighs 620 g.

III. Origami Magic Ball Skin

The skin of the robot uses the origami magic ball pattern [28], an origami structure that can transform between two physical states: an "ellipsoid" and "sphere." The pattern is a tessellation of waterbomb units, as shown in Fig. 3. When all of the units are folded and the sides of the pattern are connected to form a tube, the magic ball pattern turns into a closed, dimpled ellipsoid shape (Fig. 2). The exact shape of the folded form can be controlled by changing three main parameters: M, the number of rows of units; N, the number of columns; and s, the side length of one unit. The pattern in Fig. 3 has 4 rows and 5 columns. We call this a 4x5 magic ball for short.

The body's attainable range of aspect ratios depends on the ratio of rows to columns (M/N). When the number of rows is high, the magic ball becomes long and near-cylindrical without much capability for transformation. When the number of columns is high, the excess material around the circumference of the ball causes the pattern to buckle and fold asymmetrically. We have found experimentally that a $M : N = 2 : 5$ ratio of rows to columns generally works well for achieving large volume changes without buckling.

A. Capability for Jet Propulsion

The magic ball is a non-rigidly foldable design [28]; that is, it cannot change its shape without some deformation in the faces, particularly near the equator (ref. Fig. 5). As a result, as the ball deforms, it stores and releases strain potential energy, and it naturally tends to a lowest energy equilibrium state close to the cylindrical form that minimizes total deformation in the faces and folds.

Our robot design leverages this feature for self-propulsion. A tendon down the center of the robot compresses the ball in the longitudinal direction, adding a length constraint that forces the ball to change forms and volume and also to store internal strain energy in the folds and faces of the pattern. When the tendon is suddenly released, the ball quickly returns to its natural (ellipsoidal) equilibrium state, expelling the fluid rapidly and creating a jet.

For a jet-propelled body traveling horizontally in a fluid, the thrust force can be written as as [2]:

$$F_T = C_o \rho A_o q^2 \tag{1}$$

where q is the jet velocity, A_o is the area of the outlet (nozzle), ρ is the density of the fluid, and $C_o \leq 1$ is the frictional losses in the outlet valve. The variables A_o and C_o are constants associated with the outlet (nozzle) size. We therefore look to increase thrust by manipulating the average jet velocity. Using a simple model that jet velocity q is a function of the pressure inside the magic ball, we expect the thrust to be high when the internal pressure, or the strain energy stored in the magic ball, is high.

B. Fabrication

For this robot, we fabricated a 4x10 magic ball skin with side length $s = 88$ mm to evaluate the soft robot's ability for self propulsion. In order to make the skin easier to attach to the end caps, we used attachment tabs similar to [28] at the borders of the pattern, as shown in Fig. 3. The tabs are assembled by gluing the overlapping faces, constraining the angles between the edges of the waterbomb units at the top and bottom of the pattern. Compared to [28], we simplified the pattern by removing unneeded triangles.

To construct the skin, we cut the base pattern out of 0.102 mm (0.004") thick PET (polyethylene terephthalate) film on a PLS 4.75 (Universal Laser System) flatbed laser cutter. The boundaries of the pattern were cut as solid lines and the folds were perforated at 9 dots per cm (23 dots per inch). The blue lines connecting the tabs to the magic ball were only lightly engraved to avoid ripping. Due to the size of the pattern, the skin was cut in two pieces with 5 columns each. To connect the pieces together and seal the perforation holes, one layer of 0.015 mm (0.0006") thick PE (polyethylene) stretch wrap was adhered to the outer surface of the skin. The film was attached using 0.051 mm (0.002") thick acrylic adhesive (3M 467MP). The connecting sides between the two pieces of the pattern were reinforced with waterproof tape (3M 1522).

The magic ball was folded manually, and the overlapping triangles on the tabs were sealed together using adhesive (3M 467MP). The T-shaped tabs on the outer edges of the triangles were then clamped into custom 3D printed ABS (acrylonitrile butadiene styrene) end caps shown in Fig. 4. The tabs insert into the slots in the cap design, and four M3 flat head screws

Fig. 4. The end caps are composed of two pieces that clamp together to hold the origami skin. Left: Front cap with pieces separated. The pieces are assembled using four M3 screws (35 mm in length) and nuts. Right: The rear end cap (assembled), which serves as the nozzle, also has a cross-bar for attaching the fishing line.

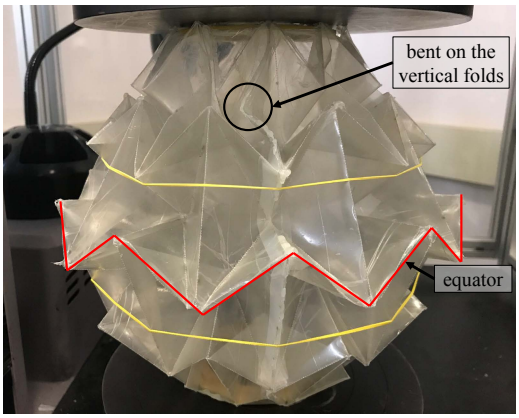

Fig. 5. Snapshot of the magic ball skin deforming under compression.

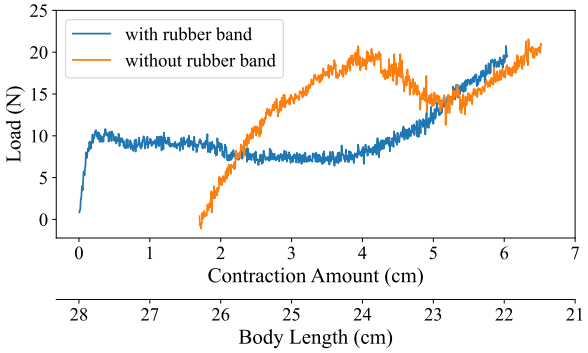

Fig. 6. Force-displacement curves for compressing the skin alone vs. with rubber bands around the circumference.

clamp the two sides of the cap to keep the pattern in place. Two rubber bands are placed around the skin in order to increase its stiffness. The entire process, including laser cutting and assembly, takes about 3 hours.

C. Force-Displacement Profile

To measure the potential energy storage in the skin, we conducted compression tests on the skin using an MTS Criterion Series 40 Load Frame with 50 kN load cell. The skin was compressed in the longitudinal direction, and was tested both in its original form and with the additional two rubber bands. The results are shown in Fig. 5 and 6. The orange curve shows the force-displacement curve of the skin without rubber bands.

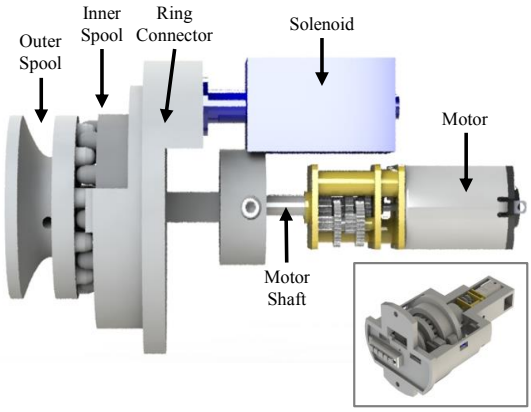

Fig. 7. The actuation mechanism consists of a spool in two parts driven by a DC motor. The inner spool is mounted to a ring connector and attached to a solenoid, which engages or disengages the teeth on the spool. The inset on the bottom right shows the fully assembled mechanism in its housing.

We removed the lid of the spine (2.5 cm in length) before the compression test to ensure a flat contact surface with the compression platen. The skin begins at a natural length of 26.3 cm, with increasing compressive force required as the skin is compressed more. We observe that there is a dip in the required force when the skin reaches a length of about 23 cm before the force continues to increase. In the physical skin, this drop in force occurs when faces near the top and bottom of the ball start to collide and the vertical folds buckle, as indicated in Fig. 5.

When rubber bands are added around the circumference of the skin, the natural state of the ball changes to be 1.7 cm longer, and the required compression forces also change. In particular, radial forces applied by the rubber bands cause the required force to rise quickly to 10 N, even at low compression amounts. In addition, due to these radial forces, the vertical folds buckle much earlier in the compression process, enabling the compressive load to remain relatively constant for the majority of the compression test. The increase in force for compression amounts greater than 4 cm is due to large amounts of deformation near the equator that appear as the skin approaches its spherical state and the folds along the equator begin to flatten out.

These trends were consistent over 4 cycles of compression of the skin. Because using rubber bands allowed us to both achieve a greater total amount of contraction and also keep compressive forces for the majority of the contraction relatively constant, we chose to include the rubber bands in the robot design.

IV. Actuation and Control

A. Tendon-Driven Actuation

The robot is driven through a tendon and spool mechanism. In order for the robot to be able to propel itself forward, the mechanism must be able to contract the robot lengthwise to pull in water and then release it quickly. This motion is achieved through the geared mechanism shown in Fig. 7. The mechanism is 3D printed in ABS.

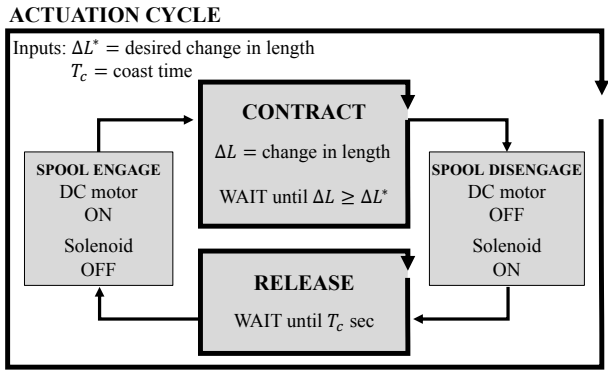

Fig. 8. Actuation cycle control flow. The robot alternately contracts its length and releases to create a jet and propel itself forward.

The main working principle behind the actuation mechanism is a geared spool with cylindrical teeth. A tendon is wrapped around an outer spool with a circumference of 4.0 cm and tied to the end cap on the rear side of the robot (Fig. 2). The inner spool is mounted to a DC motor (Pololu 1000:1 6V LP Micro Metal Gearmotor). When the teeth between the spools mesh, the motor is able to wind the tendon and contract the robot.

The inner spool is also mounted in a ring connector attached to a solenoid (Adafruit 5V Mini Push-Pull Solenoid). When the solenoid is activated, the connector and inner spool assembly is pulled to separate the teeth on the two spool pieces. The outer spool disengages and is allowed to rotate freely, causing the robot to return to its equilibrium (ellipsoidal) shape due to the inherent mechanics of the magic ball.

B. Control Electronics

The robot monitors its contraction length through a magnetic encoder attached to the outer spool, which counts the number of rotations of the spool. A radio-enabled microcontroller (Adafruit Feather M0 RFM69 Packet Radio 433 MHz) monitors the encoder reading and controls when the DC motor and solenoid are turned on and off according to the control flow in Fig. 8. In particular, the controller coordinates the motors in the spine to achieve a particular compression amount and actuation timing. In the first part of the actuation cycle, the solenoid is off to engage the spool, and the DC motor turns on to compress the robot length. The microcontroller monitors the encoder signal and waits until the estimated length change exceeds the commanded change ΔL^*. At that point, the solenoid is turned on, disengaging the spool and allowing the robot to return to its natural length at its natural speed. The robot then coasts for a predesignated amount of time T_c before the cycle is repeated. During this time, the microcontroller also monitors the encoder to check how much the spool has unwound. Note that in our setup, the speed of the motor when winding the tendon is not a control variable, so the total duration of a single actuation cycle is the amount of time needed for the motor to contract the robot's length by ΔL^*, plus T_c.

For the purposes of our experiments, a DC current sensor (Adafruit INA219) collects the electrical power input to the actuation system over the course of the robot's actuation cycle. The entire system is powered by a 7.4V 500mAh lithium-ion battery. The spine of the robot is equipped with a radio to enable tetherless data collection and command signals. The control code allows users to input the actuation parameters (ΔL^*, T_c, and the total number of actuation cycles) as serial commands, and to send start and stop signals.

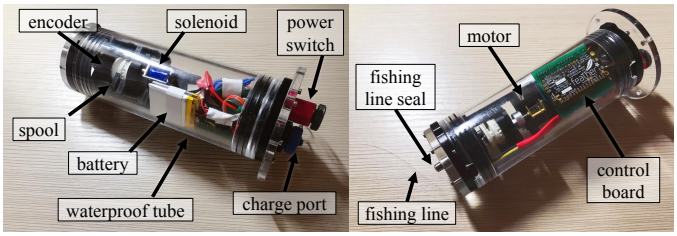

Fig. 9. The robot spine contains the actuation mechanism, control board, and battery, all stored inside a waterproof tube. An O-ring sealed outlet allows the tendon to exit the tube to connect to the rear end cap of the robot.

C. Waterproofing Enclosure

The actuation system is enclosed in a waterproof tube (Fig. 9). The Watertight Enclosure (BlueRobotics) is 15.0 cm (5.9") long with 5.08 cm (2") inner diameter and is made of cast acrylic plastic. The caps have built-in waterproofing seals. On the front of the robot, a waterproof switch and charging plug enables the robot to be turned on and off and to be charged from outside the tube. On the back of the tube, a custom seal enables the fishing line to pass from the actuation mechanism into the water without leaks.

V. Experimental Results

We tested the robot in a large water tank (4.5 m $\times$ 3 m). The robot's trajectory was tracked by an overhead high-resolution camera (GoPro HERO7 Silver, 1440p pixel resolution) mounted 2.0 m above the center of the tank. With this setup, the resolution of the camera was 0.588 cm per pixel. Colored tape (red in the front, yellow in the rear) was affixed to the end caps on the robot to simplify tracking. The videos were processed using a hue filter in OpenCV. Real-time power and encoder data were collected from the robot via radio.

With all described components, the robot floats half-submerged so that the center-line of the robot is 4.5 cm below the water surface. The nozzle in the rear end cap is fully submerged. We tested the robot with this setup to ensure a clear radio signal and video recording of the robot's motion. Weights can be added to fully submerge the robot.

A. Trajectory Analysis

In a first set of tests, the robot was commanded to execute actuation cycles with $\Delta L^* = 6.2$ cm and $T_c = 2$ s. Figure 10 shows the results. The robot was able to successfully contract and expand, and was able to move forward in the water with an average velocity of 6.70 cm/s, which translates to 0.20 body lengths/s.

Figure 10 shows the displacement of the robot's front, rear, and center of mass over time for 6 actuation cycles. The

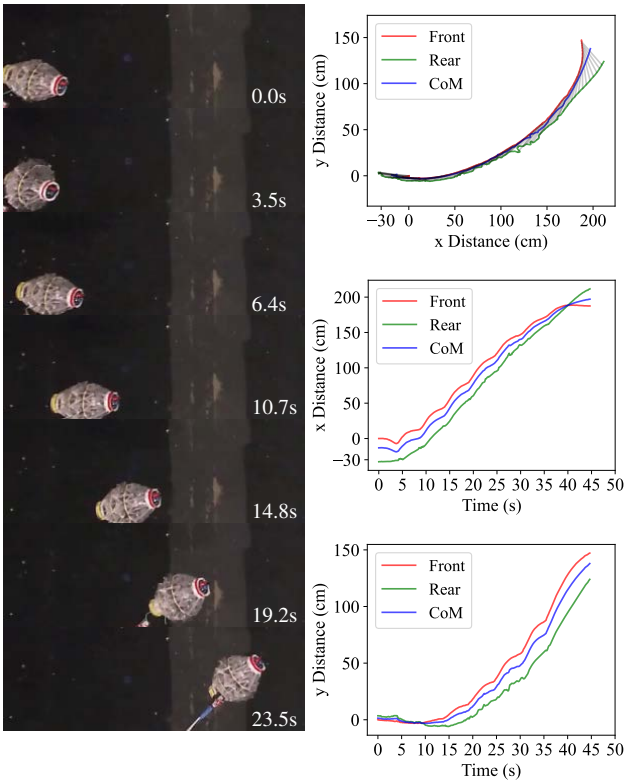

Fig. 10. Left: snapshots of the robot's motion for ($\Delta L^* = 6.2$ cm desired contraction amount, $T_c = 2$ s coast time). The robot contracts in length and releases to propel itself forward. Right: Trajectory of the front, rear, and center of mass (CoM) of the robot over time. The x-y plot (top) shows the trajectory of the robot. Gray lines show the orientation of the robot. The bottom two plots show the robot's x and y position over time.

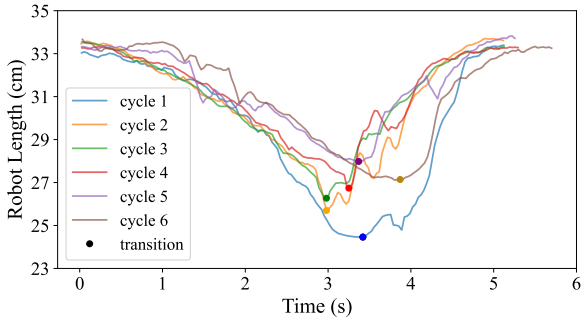

Fig. 11. Length of the robot over time for each actuation cycle with $\Delta L^* = 6.2$ cm, $T_c = 2$ s coast time. On each curve, the dot marks the time at which the robot transitioned from length contraction to release in the actuation cycle. The robot contracts in length for about 3.5 s and then releases for 2.0 s. Contraction amount was relatively consistent over all 6 actuation cycles.

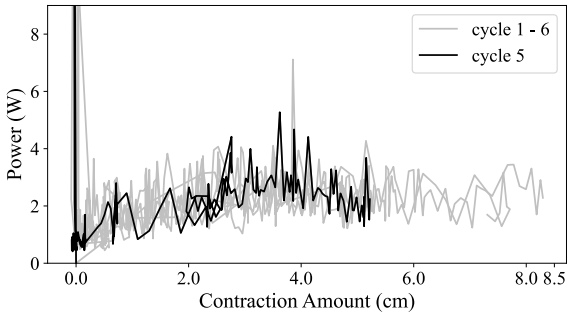

Fig. 12. Power consumption over contraction length during six actuation cycles for $\Delta L^* = 6.2$ cm, $T_c = 2$ s coast time. All cycles are shown in gray. Cycle 5 is highlighted in black for better visualization of a single trial.

data clearly slows the length change of the robot (decreasing distance between the front and read ends) over multiple actuation cycles. In addition, the trajectory data indicates that the front and center of mass experienced a back and forth motion over time, while the rear of the robot moved approximately consistently forward. The backwards portions of the trajectory coincide with the robot's "contract" stage. It is likely that during this stage, the inflow of water creates a negative pressure on the rear of the robot, in effect keeping the rear of the robot in place. When the robot expels the water during the "release" stage, the outward jet of water propels it forward. Fig. 11 shows the length of the robot over time for each actuation cycle. Contracting the robot's length takes about 3.5 s. The release phase corresponded to the commanded coast time of 2.0 s. That is, compared to the "release" stage of the actuation cycle, the length contraction happens relatively slowly, and the net effect is that the robot moves forward.

Figure 11 also shows that the length contraction for the robot is relatively consistent over actuation cycles. The robot contracted by 7.20 cm on average (minimum: 5.84 cm, maximum: 8.96 cm). This is within expected error for a commanded ΔL^* of 6.2 cm, given the resolution of the video recording and the sensors. In particular, the encoder provides 12 counts per revolution of the spool. With a spool circumference of 4.0 cm, the resolution of the length controller is thus 0.33 cm/tick. The camera resolution contributes another 0.588 cm of potential measurement error. The maximum body length captured by the camera is around 33 cm, which is about 2.5 cm longer than the robot's equilibrium length of 30.5 cm in the air. We hypothesize this extra length is produced because water has greater inertia and will add more damping than air. As a result, the flexible skin temporarily extends beyond its natural length during release as extra water exits the body.

B. Energy Consumption

Figure 12 shows the power consumption of the robot during length contraction, as measured by the current sensor in the robot spine. Initial spikes in the power consumption correspond to the motor starting up at the beginning of the cycle. The power consumption is relatively flat, matching the force-displacement curve measured for the robot skin in Fig. 6 for low contraction amounts. For high contraction amounts above 4 cm, the two curves diverge. In particular, in MTS tests, we observed an increase in required compressive force, while the power curve on the robot remains relatively flat. This difference may be caused by the water flowing into the skin, which will add inertia and damping to the system and may impact precisely how the faces and folds in the skin deform. We will further investigate these differences in future work.

Integrating the area under the power curve indicates that the average energy consumption of the robot over an actuation cycle was 5.91 J. We compute the cost of transport as

Table I
RESULTS FOR VARYING CONTRACTION AMOUNT (ΔL^*)

ΔL^* (cm)	T_c (s)	Cycles	Contraction (cm)	Energy (J)	Velocity (cm/s)	Cost of transport
4.3	2	5	1.84	2.48	2.29	3.87
5.5	2	5	4.46	4.41	5.02	2.42
6.2	2	6	7.20	5.91	6.70	2.00

All tests conducted with $T_c = 2$ s

Table II
RESULTS FOR VARYING COAST TIME (T_c)

ΔL^* (cm)	T_c (s)	Cycles	Contraction (cm)	Energy (J)	Velocity (cm/s)	Cost of transport
6.2	1	5	4.52	5.75	5.75	3.76
6.2	2	6	7.20	5.91	6.70	2.00
6.2	3	5	6.92	5.21	6.50	2.06

All tests conducted with $\Delta L^* = 6.2$ cm

CoT $= E/(mgd)$ where E is the electromechanical energy used by the robot, m is the mass of the robot, d is the total distance travelled, and g is acceleration due to gravity. The cost of transport of the robot for this set of trials was 2.00. This value is slightly higher than biological squids of the same weight [29] and other squid-inspired robots, which achieve a COT ranging from 0.087 to 1.3 [30].

C. Variations in Actuation Parameters

We explored the effect of the actuation parameters on the robot's performance. In general, for all tests, the robot followed the same pattern of forward and backward motion.

Table I reports the mean contraction amount, total energy consumption, mean velocity, and cost of transport for varying contraction amounts with coast time $T_c = 2$ s. The commanded length changes were $\Delta L^* = \{4.3, 5.5, 6.2\}$ cm. When $\Delta L^* = 6.2$ cm, the robot is fully compressed, i.e., the spine hits the end cap so that the robot cannot be compressed any further. From the data, the robot was able to consistently achieve the desired contraction amount within measurement error, although the contraction for the $\Delta L^* = 4.3$ cm experiment was lower than expected. Comparing to true contraction, it seems clear that there is a high dependency of average velocity on contraction amount. This makes sense since higher contraction amounts not only corresponded to higher robot volumes, but also to higher contraction forces, resulting in longer, higher-speed output jets. In general, when the contraction amount increases, more energy is required for the motor to contract the robot, but since the average velocity also increases, leading to an overall lower cost of transport. This effect, however, would of course depend on the particular pattern design.

Table II shows the results for varying coast times ($T_c = \{1, 2, 3\}$ s) with a length change of $\Delta L^* = 6.2$ cm. It is interesting to note that for short coast times ($T_c = 1$ s), the contraction amount was significantly lower than the expected value. We hypothesize that the reason for this is that the robot does not have enough time to return completely to its original length. As a result, its maximum length is shorter than the other experimental runs, and, further, the velocity is also reduced. This relationship between the frequency and swimmer speed agrees with existing work [16], [31]. At the same time, all three experimental conditions consumed approximately the same energy. Although the $T_c = 1$ s condition was contracting by a smaller amount, the contraction that did occur was at lower lengths (i.e., higher force portions of the force-displacement curve), reducing energy savings. Further, we noticed higher power spikes at the beginning of the actuation cycles for $T_c = 1$ s trials, further supporting that the robot was still returning to its natural length when the actuation cycle began again.

VI. CONCLUSIONS

In this paper, we demonstrated a jet-propelled origami-inspired swimming robot capable of swimming with an average speed of up to 6.70 cm/s (0.20 body lengths per second). The robot leverages an origami skin that morphs from an ellipsoidal shape to a spherical shape upon compressing its length. The pattern stores internal strain energy in the faces and folds of the pattern, allowing it to rapidly release the water inside the body to propel the robot to swim forward. Our experiments on the robot indicate that the speed and cost of transport of the robot change as the contraction amount of the robot and the actuation frequency. The results indicate that the origami swimmer robot could be a relatively power efficient cephalopod-inspired robot.

However, several design improvements can be made to make the robot more powerful and robust. There is an 18% to 24% variation in the contraction amount for the robot. It is possible that some of this error is accounted for by stretching in the fishing line over time. As the fishing line stretches, the commanded contraction length (ΔL^*) may not accurately represent the actual length change of the robot. We changed out the fishing line multiple times over the course of the experiment, but future work includes updating the fishing line spooling design to reduce this effect.

Additional experiments are also required in order to more fully characterize the robot's performance. Our experiments swept three contraction values and three actuation frequencies, and our results indicated that higher contraction amounts and lower actuation frequencies improved the cost of transport. We expect that for any given robot skin, there would exist optimal actuation parameters. Swimming is a complex behavior that is affected not only by the robot's mass, geometry, and potential thrust output, but also additional hydrodynamic effects such as the added mass effect, pressure gradients stemming from the rate of shape change, and more [32]. Our results are slightly limited by the small number of actuation cycles used for calculations. The robot took about 3 actuation cycles to ramp up to a steady state velocity (at which point it was approaching the boundaries of the tank). Future work would include a systematic study of the robot's behavior under a wider range of parameters with longer trials.

The design of the robot aims for easy replacement of the skin. The skin itself is also fast to manufacture and can be assembled with in a few hours. Of particular interest would be the effect of the skin design (both its geometric and its mechanics properties) on the robot's locomotion. Empirically, different magic ball parameters have an affect on the pattern's achievable aspect ratios and its force-displacement curve. Further, it is also likely that the roughness of the skin will affect the robot's drag coefficient and its cost of transport. Radial perturbations can be seen when the robot transitions between length contraction and release phases of its actuation cycle, indicating that the robot is not utilizing its deformation as effectively as possible. This means that changing the resolution or dimension of the skin could cause a difference in the swimming performance and efficiency. We plan to modify the pattern by tuning the number of rows and columns, thereby changing the overall size and roughness of the pattern, to characterize their effect on the robot's energy efficiency in future work.

ACKNOWLEDGMENT

The authors would like to thank Gedaliah Knizhnik and Dr. Ani Hsieh for their assistance with setting up the swimming experiments, Terry Kientz for his assistance on the waterproofed enclosure design, Jeremy Wang for his assistance on 3D printing, Emily Wang for her assistance with the fabrication of the origami skin, Guoyao Shen for his assistance in designing the robot's control board, and Gnana Saurya Vankayalapati, Dr. Kevin Turner, and Peter Bruno for their assistance with MTS measurements.

REFERENCES

[1] E. J. Anderson and M. E. DeMont, "Mechanics of squid locomotion," *The Journal of Experimental Biology*, vol. 203, pp. 2851–2863, 2000.

[2] W. Johnson, P. Soden, and E. Trueman, "A study in jet propulsion: an analysis of the motion of the squid, *Loligo vulgaris*," *Journal of Experimental Biology*, vol. 56, no. 1, p. 155–165, 1972.

[3] S. Steele, G. Weymouth, and M. Triantafyllou, "Added mass energy recovery of octopus-inspired shape change," *Journal of Fluid Mechanics*, vol. 810, pp. 155–174, 2017.

[4] L. A. Ruis, R. W. Whittlesey, and J. O. Dabiri, "Vortex-enhanced propulsion," *Journal of Fluid Mechanics*, vol. 668, p. 5–32, 2011.

[5] M. Gharib, E. Rambod, and K. Shariff, "A universal time scale for vortex ring formation," *Journal of Fluid Mechanics*, vol. 360, p. 121–140, 1998.

[6] P. S. Krueger and M. Gharib, "The significance of vortex ring formation to the impulse and thrust of a starting jet," *Physics of Fluids*, vol. 15, no. 5, pp. 1271–1281, 2003.

[7] I. K. Bartol, P. S. Krueger, W. J. Stewart, and J. T. Thompson, "Hydrodynamics of pulsed jetting in juvenile and adult brief squid Lolliguncula brevis: evidence of multiple jet 'modes' and their implications for propulsive efficiency," *Journal of Experimental Biology*, vol. 212, no. 12, pp. 1889–1903, 2009.

[8] M. Krieg and K. Mohseni, "On approximating the translational velocity of vortex rings," *Journal of Fluids Engineering-transactions of The Asme*, vol. 135, p. 124501, 2013.

[9] A. K. L. F. Giorgio-Serchi and G. D. Weymouth, "A soft aquatic actuator for unsteady peak power amplification," *IEEE/ASME Transactions on Mechatronics*, vol. 23, no. 6, pp. 2968–2973, 2018.

[10] G. D. Weymouth and M. S. Triantafyllou, "Ultra-fast escape of a deformable jet-propelled body," *Journal of Fluid Mechanics*, vol. 721, p. 367–385, 2013.

[11] Y. Chen, H. Wang, E. F. Helbling, N. T. Jafferis, R. Zufferey, A. Ong, K. Ma, N. Gravish, P. Chirarattananon, M. Kovac, *et al.*, "A biologically inspired, flapping-wing, hybrid aerial-aquatic microrobot," *Science Robotics*, vol. 2, no. 11, p. eaao5619, 2017.

[12] T. Chen, O. R. Bilal, K. Shea, and C. Daraio, "Harnessing bistability for directional propulsion of soft, untethered robots," *Proceedings of the National Academy of Sciences*, vol. 115, no. 22, pp. 5698–5702, 2018.

[13] A. D. Marchese, C. D. Onal, and D. Rus, "Autonomous soft robotic fish capable of escape maneuvers using fluidic elastomer actuators," *Soft Robotics*, vol. 1, no. 1, pp. 75–87, 3 2014.

[14] H. Yuk, S. Lin, C. Ma, M. Takaffoli, N. X. Fang, and X. Zhao, "Hydraulic hydrogel actuators and robots optically and sonically camouflaged in water," *Nature Communications*, vol. 8, p. 14230, 2017.

[15] R. K. Katzschmann, J. DelPreto, R. MacCurdy, and D. Rus, "Exploration of underwater life with an acoustically controlled soft robotic fish," *Science Robotics*, vol. 3, no. 16, p. eaar3449, 2018.

[16] F. G. Serchi, A. Arienti, I. Baldoli, and C. Laschi, "An elastic pulsed-jet thruster for soft unmanned underwater vehicles," in *IEEE International Conference on Robotics and Automation*, 2013, pp. 5103–5110.

[17] C. Christianson, Y. Cui, M. Ishida, X. Bi, Q. Zhu, G. Pawlak, and M. T. Tolley, "Cephalopod-inspired robot capable of cyclic jet propulsion through shape change," *Bioinspiration & Biomimetics*, vol. 16, no. 1, p. 016014, 2020.

[18] S. Kim, C. Laschi, and B. Trimmer, "Soft robotics: a bioinspired evolution in robotics," *Trends in Biotechnology*, vol. 31, no. 5, pp. 287–294, 2013.

[19] G. D. Weymouth, V. Subramaniam, and M. S. Triantafyllou, "Ultra-fast escape maneuver of an octopus-inspired robot," *Bioinspiration & Biomimetics*, vol. 10, no. 1, p. 016016, 2015.

[20] K. Arakawa, F. Giorgio-Serchi, and H. Mochiyama, "Snap pump: A snap-through mechanism for a pulsatile pump," *IEEE Robotics and Automation Letters*, vol. 6, no. 2, pp. 803–810, 2021.

[21] F. Giorgio-Serchi, A. Arienti, and C. Laschi, "Underwater soft-bodied pulsed-jet thrusters: Actuator modeling and performance profiling," *The International Journal of Robotics Research*, vol. 35, no. 11, pp. 1308–1329, 2016.

[22] Z. Shen, J. Na, and Z. Wang, "A biomimetic underwater soft robot inspired by cephalopod mollusc," *IEEE Robotics and Automation Letters*, vol. 2, no. 4, pp. 2217–2223, 2017.

[23] T. Wang, A. K. Lidtke, F. Giorgio-Serchi, and G. D. Weymouth, "Manoeuvring of an aquatic soft robot using thrust-vectoring," in *IEEE International Conference on Soft Robotics (RoboSoft)*, 2019, pp. 186–191.

[24] T. Cheng, G. Li, Y. Liang, M. Zhang, B. Liu, T.-W. Wong, J. Forman, M. Chen, G. Wang, Y. Tao, and T. Li, "Untethered soft robotic jellyfish," *Smart Materials and Structures*, vol. 28, no. 1, p. 015019, 2018.

[25] C. Sung and D. Rus, "Foldable joints for foldable robots," *Journal of Mechanisms and Robotics*, vol. 7, no. 2, p. 021012, 2015.

[26] D. Rus and M. T. Tolley, "Design, fabrication and control of origami robots," *Nature Reviews Materials*, vol. 3, no. 6, pp. 101–112, 2018.

[27] J. L. Silverberg, A. A. Evans, L. McLeod, R. C. Hayward, T. Hull, C. D. Santangelo, and I. Cohen, "Using origami design principles to fold reprogrammable mechanical metamaterials," *Science*, vol. 345, no. 6197, pp. 647–650, 2014.

[28] D.-Y. Lee, S.-R. Kim, J.-S. Kim, J.-J. Park, and K.-J. Cho, "Origami wheel transformer: A variable-diameter wheel drive robot using an origami structure," *Soft Robotics*, vol. 4, no. 2, pp. 163–180, 2017.

[29] B. J. Gemmell, J. H. Costello, S. P. Colin, C. J. Stewart, J. O. Dabiri, D. Tafti, and S. Priya, "Passive energy recapture in jellyfish contributes to propulsive advantage over other metazoans," *Proceedings of the National Academy of Sciences*, vol. 110, no. 44, pp. 17 904–17 909, 2013.

[30] T. Bujard, F. Giorgio-Serchi, and G. D. Weymouth, "A resonant squid-inspired robot unlocks biological propulsive efficiency," *Science Robotics*, vol. 6, no. 50, 2021.

[31] F. Giorgio-Serchi, F. Renda, M. Calisti, and C. Laschi, "Thrust depletion at high pulsation frequencies in underactuated, soft-bodied, pulsed-jet vehicles," *OCEANS 2015 - Genova*, pp. 1–6, 2015.

[32] J. H. Cartwright, U. Feudel, G. Károlyi, A. de Moura, O. Piro, and T. Tél, "Dynamics of finite-size particles in chaotic fluid flows," in *Nonlinear Dynamics and Chaos: Advances and Perspectives*. Springer, 2010, pp. 51–87.